OPEN ACCESS
IOP Publishing | National Institute for Materials Science
Science and Technology of Advanced Materials
Sci. Technol. Adv. Mater. **15** (2014) 015004 (11pp)
doi:10.1088/1468-6996/15/1/015004

# Studying nanostructure gradients in injection-molded polypropylene/ montmorillonite composites by microbeam small-angle x-ray scattering

**Norbert Stribeck[1], Konrad Schneider[2], Ahmad Zeinolebadi[3], Xuke Li[1], Catalina-Gabriela Sanporean[4], Zina Vuluga[5], Stela Iancu[5], Monica Duldner[5], Gonzalo Santoro[6] and Stephan V Roth[6]**

[1] Department of Chemistry, Institute TMC, University of Hamburg, Bundesstrasse 45, D-20146 Hamburg, Germany
[2] Leibniz-Institut für Polymerforschung (IPF), D-01069 Dresden, Germany
[3] Polymer Consult Ltd, Dorfgrund 6, D-22397 Hamburg, Germany
[4] Department of Mechanical and Manufacturing Engineering, Aalborg University, Fibigerstræde 16, DK-9220 Aalborg, Denmark
[5] National Research and Development Institute of Chemistry and Petrochemistry ICECHIM, Splaiul Independentei 202, Bucharest, Romania
[6] HASYLAB at DESY, Notkestraße 85, D-22603 Hamburg, Germany

E-mail: norbert@stribeck.de

Received 22 October 2013
Accepted for publication 24 December 2013
Published 17 January 2014

**Abstract**

The core–shell structure in oriented cylindrical rods of polypropylene (PP) and nanoclay composites (NCs) from PP and montmorillonite (MMT) is studied by microbeam small-angle x-ray scattering (SAXS). The structure of neat PP is almost homogeneous across the rod showing regular semicrystalline stacks. In the NCs the discrete SAXS of arranged crystalline PP domains is limited to a skin zone of 300 $\mu$m thickness. Even there only frozen-in primary lamellae are detected. The core of the NCs is dominated by diffuse scattering from crystalline domains placed at random. The SAXS of the MMT flakes exhibits a complex skin–core gradient. Both the direction of the symmetry axis and the apparent perfection of flake-orientation are varying. Thus there is no local fiber symmetry, and the structure gradient cannot be reconstructed from a scan across the full rod. To overcome the problem the rods are machined. Scans across the residual webs are performed. For the first time webs have been carved out in two principal directions. Comparison of the corresponding two sets of SAXS patterns demonstrates the complexity of the MMT orientation. Close to the surface ($<1$ mm) the flakes cling to the wall. The variation of the orientation distribution widths indicates the presence of both MMT flakes and grains. The grains have not been oriented in the flowing melt. An empirical equation is presented which describes the variation from skin to core of one component of the inclination angle of flake-shaped phyllosilicate filler particles.

Keywords: polypropylene, layered silicate, injection-molded, skin–core, orientation, x-ray scattering

## 1. Introduction

### *1.1. Composites to improve materials properties*

Polyolefins are widely used as structural materials. In automotive they can reduce fuel consumption, because they are lighter than metal. Their favorable mechanical properties are based on their unique semicrystalline nanostructure. It is characterized by shape and arrangement of the crystalline domains within in the amorphous matrix. Nevertheless, the materials properties of polypropylene (PP) must be improved, before more metal can be replaced by plastics. One of the goals is a reduced fatigue. To achieve such an improvement, nanoclay composites (NCs) of layered silicates and PP are made. Respective studies are frequently reported [1] in the literature. However, the practical applicability of PP/MMT composites still appears to be low [2, 3].

### *1.2. Compatibilization and nucleation*

Frequently the reinforcing phyllosilicate is a modified montmorillonite (MMT). By melt-mixing exfoliated MMT with PP a nanocomposite is obtained. Recent reviews summarize [3–6] that modifications of the MMT are predominantly focusing on an improvement of the compatibility between the clay and the polyolefin. What is often not taken into account is, that many phyllosilicates nucleate [7–14] PP extremely well. An altered nucleation may change the resulting semicrystalline structure considerably [15–19]. The nucleating sites of the phyllosilicate are reported to be the gallery gaps between the clay layers [10], and the nucleation efficiency is said to depend on origin and treatment of the layered silicate. For example, partial [20, 21] exfoliation of the MMT even increases [22–24] the nucleation efficiency of MMT in PP. Regarding the PP nanostructure it is reported [9] that addition of MMT accelerates the crystallization considerably and lowers the crystallinity somewhat. This observation is related to a raised density of heterogeneous nuclei in the composite that prevents the individual crystalline layers to grow up to their regular size. Poor material properties correlate with high nucleation efficiency of the mineral filler [8]. In such materials the reinforcing effect of the MMT filler appears consumed [25] by weakening of the PP matrix.

### *1.3. SAXS studies on PP/phyllosilicate composites*

Small-angle x-ray scattering (SAXS) is an important method for the investigation of semicrystalline nanostructure. In contrast, wide-angle x-ray scattering appears to be of secondary importance because it only probes the properties of crystallites, i.e. of the building blocks of the crystalline domains. With respect to PP-based nanocomposites SAXS is rarely applied. Employed on isotropic [5, 11] samples, the information content remains quite low. It is reported [11] that MMT nucleates PP and that in the nanocomposite the average distance between the crystalline lamellae is longer than in the neat PP.

A study of fibers [26] shows the equatorial scattering of MMT, but no discrete scattering of the PP. In a SAXS study that monitors the structure evolution of compression-molded material under mechanical load [27] the distance between sample and detector is too long to detect the phyllosilicate scattering. Here both the neat PP and the nanocomposite show an isotropic reflection of well-crystallized PP.

Our group has published two SAXS studies [25, 28] on different injection-molded PP/MMT materials under mechanical load. The mechanical properties of the composites and of the neat PP have been similar, but the semicrystalline structure of the PP and its response to load have been different. In both studies the MMT scattering has not been observed because of technical restrictions. Nevertheless, the different responses of the nanostructures to the load have indicated that intense heterogeneous nucleation by MMT has weakened the semicrystalline structure of the PP.

### *1.4. From macrobeam to microbeam*

In order to visualize the MMT scattering together with the scattering of the PP we have now moved from a macrofocus beamline to a microfocus beamline. Here a much wider range of angles is mapped on a single detector than on a macrofocus beamline [29, 30]. In addition, the microbeam can be used to scan [31–34] across the sample in small steps. Thus the skin–core structure gradient of an injection-molded part can be studied. If the symmetry of the sample structure is favorable, mechanical machining of the cylindrical sample is not necessary and the structure gradient can be reconstructed form the series of SAXS patterns by computed tomography [35, 36]. Similar simple fiber symmetry is implicitly assumed, whenever orientation distributions are quantified by computation of the uniaxial orientation parameter (UOP) (Hermans *et al* [37]). Unfortunately, the studied NCs do not obey simple fiber symmetry.

### *1.5. Filler orientation*

We are aware of several practical studies of the orientation of filler particles in composites. Wang and Cakmak [38] examine the skin–core structure of injection-molded poly(vinylidene fluoride) (PVDF) test bars using an x-ray microbeam. They apply both wide-angle x-ray diffraction (WAXD) and SAXS. For the WAXD survey they adapt the pole-figure method. The SAXS method is used to demonstrate the skin–core gradient of the semicrystalline PVDF structure. All the patterns of the neat PVDF taken along the cut exhibit simple fiber symmetry: uniaxial symmetry of all the patterns with their axes parallel to the flow direction.

An early study on injection-molded glass-fiber reinforced PP [39] applies an UOP analysis to data extracted from scanning-electron-microscopy (SEM) pictures. It quantifies the orientation of the filler particles as a function of the depth below the skin. Another experimental paper [40] is dedicated to the study of composites made from thermoplastic polyurethane and carbon nanotubes (CNT). Again, the UOP is computed from the x-ray scattering data to quantify the CNT orientation. Xavier *et al* [41] study injection-molded bars of PP/mica nanocomposites and determine the orientation of the mica flakes from SEM images. They report that close

to the surface the mica flakes cling to the wall. The authors discuss the effect of the flake orientation on the mechanical properties. Altan [42] reviews both the technical process of injection molding for fiber-reinforced composites, and several mathematical models for filler-particle orientation. The models can also be applied to flake-shaped filler particles. Analytical solutions are only known for very simple cases. Nevertheless, numerical predictions are sketched in Altan's paper.

### *1.6. Orientation and materials properties*

Two theoretical papers [43, 44] that relate filler-particle orientation to mechanical properties are frequently cited. There are no analytical solutions for the given constitutive equations. An experimental paper [45] on injection-molded neat PP reports the chain orientation and correlates high orientation in the skin layer with improved material properties. In our present study we are not yet able to relate the orientation of MMT flakes to the properties, but an empirical equation (equation (1)) extracted from the scattering data might become helpful in future modeling and prediction of materials properties.

## 2. Experimental

### *2.1. Materials*

Composites of PP, linear poly(styrene–(ethylene-co-butylene) –styrene) block copolymer (SEBS) and MMT are studied. The PP grade is Moplen® HP400R (Lyondell Basell) with a melt flow index (MFI) of 25 g per 10 min (230 °C per 2.16 kg) and a density of 0.900 g cm$^{-3}$. The SEBS triblock copolymer is Kraton® 1652 G SQR 1000. Its MFI is 5.00 g per 10 min (230 °C per 5 kg). The total polystyrene content is 30 wt%. Each of the blocks has a molar mass $M_n = 79.1\,\mathrm{kg\,mol^{-1}}$. SEBS is added both as impact modifier and as a potential compatibilizer [46]. The MMT is a modified Dellite® 67G (mD67G, provided by Laviosa Chimica Mineraria). mD67G is a MMT organophilized by a cation exchange reaction with dimethyl dihydrogenated tallow ammonium chloride. It has a cation exchange capacity of 125 meq per 100 g. In a second step this MMT is modified by oligoester ionomer compounds derived from chemical processing of poly(ethylene terephthalate) waste. Two different compounds are added. One NC contains the technical compound. Another composite contains a purified compound in which the OH functionalization degree has been reduced from 150 to 110 mgKOH g$^{-1}$. This has been achieved by removing the free glycols from the precursor oligomer ionomer. The compositions of the prepared samples are reported in table 1. Sample NC_A_20p contains MMT modified by the purified oligoester ionomer compound.

The components are mixed in a DSE 20 Brabender twin screw extruder (screw diameter 20 mm, aspect ratio 40 and six heating zones), at 175 °C and 220 rpm screw rotation speed. Neat PP is processed under the same conditions. After extrusion, the strands are chopped and used for preparation of cylindrical rods of 3 mm diameter. The rods are injection molded in a laboratory injection-molding machine (MiniJet II, Thermo Scientific) from a melt of 200 °C. Mold temperature is 30 °C, molding pressure is 650 bar, molding time is 45 s, holding pressure is 100 bar and holding time is 20 s.

**Table 1.** NCs based on isotactic PP and organophilized MMT (mD67G). The sample coding is identical to that from earlier work [28]. Digits in the labels indicate the content of SEBS copolymer. $w_{c,PP}$ is the weight crystallinity of the PP component as determined by differential scanning calorimetry (cf [28]).

| Sample | PP/SEBS/mD67G (wt%) | $w_{c,PP}$ (%) |
|---|---|---|
| PP_A | 100/0/0 | 44 |
| NC_A_12 | 75/12/13 | 43 |
| NC_A_20 | 67/20/13 | 41 |
| NC_A_20p | 67/20/13 | 41 |

The resulting polymer rods are highly oriented. This fact is not only a function of the processing conditions but also of the molecular weight distribution of the PP [47]. For this commercial product an average molecular weight and the polydispersity are unknown, but the resulting high orientation indicates the presence of sufficiently long chains (high entanglement density).

*2.1.1. Machining of the rods.* The aim is to study the nanostructure gradient along the radii of the injection-molded cylinders by x-ray scattering. If the full cylindrical sample is scanned by a microbeam, the recorded scattering patterns are not directly related to the nanostructure sought after. Instead, they represent a superposition of the structure gradient along the path of the microbeam in the sample. Nevertheless, under certain conditions a computed-tomographic method [35, 36, 48, 49] can be utilized that desmears the scattering patterns from such 'tomo-scans' mathematically. Necessary assumptions for such 'mathematical machining' are, firstly, the presence of fiber symmetry in each volume element ('voxel') of the material (the voxel size given by the step-size of the scan) and secondly, the fiber axis must stay nearly parallel to the cylinder axis everywhere. The last condition is not met with the studied NCs. Therefore the rods have been machined and the residual webs have been irradiated by the microbeam. Figure 1 shows photos of some of the machined samples. The different microbeam scans are indicated by sequences of dots. Data from tomo-scans would have to be reconstructed. P- and n-scans view the voxels from different directions. P-scan means 'parallel scan'. When the microbeam first hits the sample, it runs parallel to the wall of the cylinder. N-scan means 'normal scan'. When the microbeam first hits the sample at the top, it traverses in normal direction through the wall of the cylinder. To our knowledge, n-scans have never before been carried out. For samples with local fiber symmetry the p- and the n-scans should show an identical evolution. Step size of the horizontal scans (tomo-scans and p-scans) is 0.1 mm. Because the angle of the slanted web is 63°, the suitable step size chosen for the n-scans is 0.2 mm ($\arctan 63° \approx 2$).

*2.1.2. SAXS setup.* SAXS is carried out in the synchrotron beamline P03 at HASYLAB, Hamburg, Germany with a

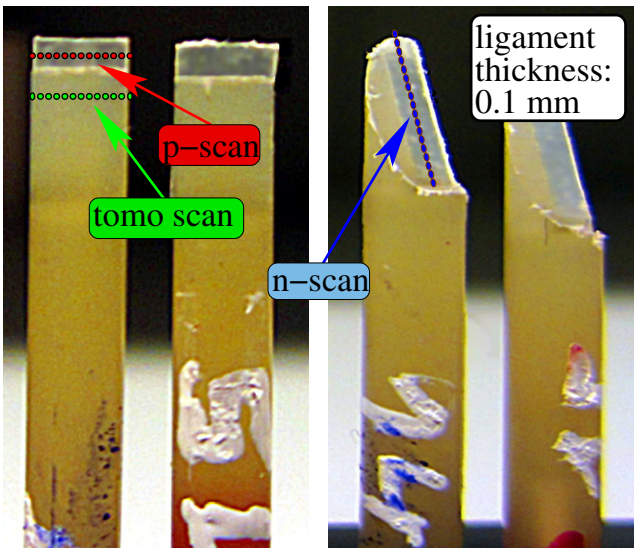


**Figure 1.** Samples machined by a computerized numerical control cutter in order to access the radial structure gradient directly in scans. P-scan across a horizontal ('dash –') central web of 0.1 mm thickness. N-scan along a slanted ('slash /') web of 0.1 mm thickness. Tomo scan: across the full rod. Tomo-scan data must be desmeared making assumptions.

microfocus beam of size 38 $\mu$m × 19 $\mu$m. The wavelength of radiation is $\lambda = 0.109$ nm and the sample–detector distance is 2640 mm. Scattering patterns are collected by a 2D PILATUS 1M detector (DECTRIS Ltd, Baden, Switzerland) with 981×1043 pixels (pixel size: 172 $\mu$m × 172 $\mu$m). The samples are translated through the microbeam stepwise, and SAXS patterns are recorded at each step. The exposure time is 10 s. The intensity of the beam before and after the sample is monitored. The machine background is recorded before each sample scan (for determination of the absorption factor and machine background subtraction). The patterns $I(\mathbf{s}) = I(s_{12}, s_3)$ cover the region $0.006\,18 \leqslant |s_{12}, s_3| \leqslant 0.42\,\mathrm{nm}^{-1}$. $\mathbf{s} = (s_{12}, s_3)$ is the scattering vector with its modulus defined by $|\mathbf{s}| = s = (2/\lambda)\sin\theta$. $2\theta$ is the scattering angle. $s_3$ is the local fiber axis. In real space the monitored area corresponds to $160 \geqslant |r_{12}, r_3| \geqslant 2.4$ nm. The scattering patterns are normalized and background corrected [50]. This means intensity normalization for constant primary beam flux, zero absorption and constant irradiated volume $V_0$. Radiation damage has been checked by taking SAXS patterns from the same spot repeatedly. Up to an exposure of 3 min no radiation damage has been detected.

*2.1.3. Bridging blind areas on the detector.* A PILATUS detector is composed of sensitive tiles separated by blind gaps. Some of the blind areas can be filled exploiting the four-quadrant symmetry of SAXS patterns with fiber symmetry. For filling the remaining 'cheese holes', data have been extrapolated assuming that SAXS patterns do not show sharp reflections which may hide in such a hole. The extrapolation is based on a radial basis function [51] representation. A flow chart of the newly designed hole-filling algorithm is presented in figure 2. The border-tracing algorithm for hole detection is described in the Worldwide

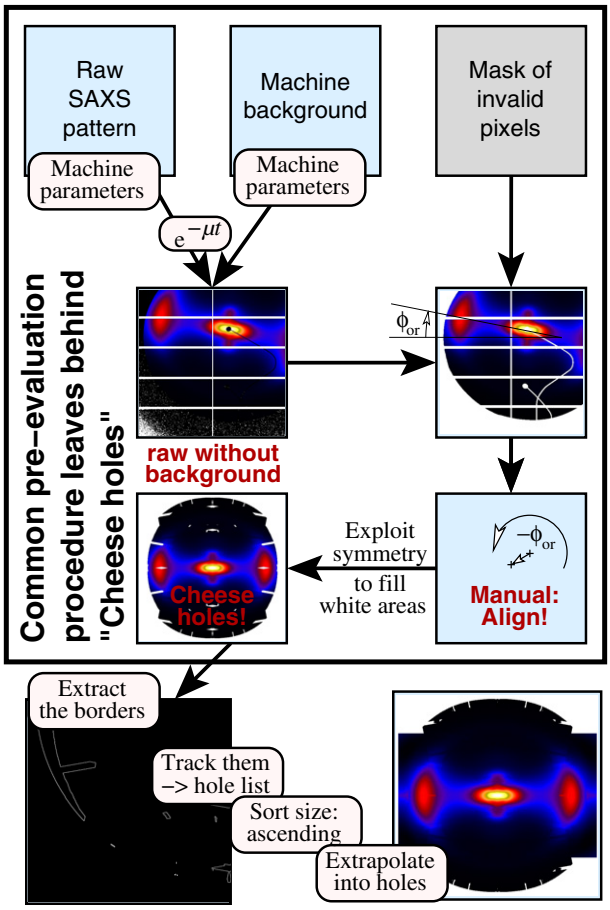


**Figure 2.** For fiber patterns from a PILATUS detector the common pre-evaluation method (big frame) leaves behind 'cheese holes'. They can be automatically detected by border tracing yielding a hole-list. Then each hole is filled by two-dimensional (2D) extrapolation starting from the smallest hole.

Web[7] [52]. A corresponding library function 'bwboundaries' is part of MATLAB [53]. For our evaluation the algorithm has been implemented in PV-WAVE [54]. In figure 2 the box 'Manual Align' indicates a misorientation angle $\phi_{\mathrm{or}}$. $\phi_{\mathrm{corr}} = -\phi_{\mathrm{or}}$ is the angle by which fiber axis of the pattern must be rotated to make it point in vertical direction. Only if $\phi_{\mathrm{or}}$ is constant for all the patterns from a scan it may be meaningful to apply computed tomography. In the favorable case $\phi_{\mathrm{or}}$ only corrects the tilt between the sample orientation and the detector orientation. Working with a tilted detector helps with the filling of blind areas.

Although the multidimensional chord distribution function (CDF) [55], $z(\mathbf{r})$, has been computed from each of the patterns $I(\mathbf{s}) = I(s_{12}, s_3)$, it is not discussed here. The reason is, that the NCs only show a rudimental discrete SAXS in only a thin surface layer of the rods that is readily explained by PP quenched from the melt during primary crystallization. All the patterns from the core of the molded rods show only the scattering of perfectly stacked MMT layers. For perfect lattice-like structures a CDF analysis does not return a more

[7] Border tracing—digital image processing lectures (www.engineering.uiowa.edu/~dip/LECTURE/Segmentation2.html#tracing).

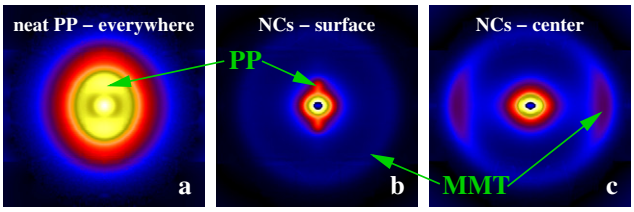


**Figure 3.** SAXS patterns from n-scans ('slash') displaying the typical features. (a) The neat PP rod shows almost the same pattern everywhere for all kinds of scans (p-scan, n-scan and tomo-scan). The arrow points at the long-period reflection of the semicrystalline structure. (b) The NCs show only at the rod surface discrete SAXS from both the PP and the MMT. (c) Inside the NC-rods only discrete scattering of the MMT is observed. The local fiber axis ($s_3$) is vertical. The patterns show log (log ($I$ ($s_{12}$, $s_3$))) in the region $-0.38 \leqslant s_{12}, s_3 \leqslant 0.38\,\mathrm{nm}^{-1}$.

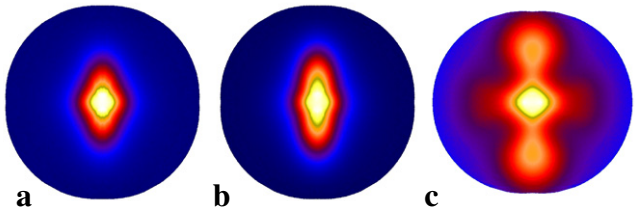


**Figure 4.** Typical structure formation steps of neat PP during oriented isothermal crystallization observed by SAXS [57]. (a) Short meridional streak. Primary crystallization has started by placement of oriented layers at random but generally long distances. (b) Longer meridional streak. The interval of random distances now covers shorter spacings, as well. (c) Secondary crystallization has finished. Secondary lamellae have 'parked' in the center of the gaps between the primary ones and this regularity has generated the peak.

detailed view on the nanostructure than a direct analysis of the scattering peak.

## 3. Results and discussion

### *3.1. Characteristic SAXS patterns and the semicrystalline PP structure*

Although the SAXS patterns of the NCs vary considerably along the radius of the molded rods, the number of their characteristic features is very limited. In particular no discrete scattering of the SEBS is observed. The typical discrete pattern of SEBS containing 30 wt% of polystyrene shows a modulated layer line above and below the equator [56]. Figure 3 presents typical SAXS patterns in pseudo-color plots of log (log ($I$ ($s_{12}$, $s_3$))). This scaling has been chosen to simultaneously visualize features of strongly differing intensity. In a previous paper [28] dedicated to the investigation of fatigue under mechanical load-cycling we have used a macrobeam and thus recorded SAXS patterns averaged over the complete cross-section of the rod-shaped sample. The corresponding patterns look similar to the new microbeam patterns from the skin region. Nevertheless, the MMT scattering had not been accessible in the macrobeam study in which the monitored region corresponded to only $60 \geqslant |r_{12}, r_3| \geqslant 4.5$ nm in real space.

Figure 3(a) shows the SAXS pattern of neat PP. The polymer has crystallized in a highly oriented state. The long-period peak (arrow) has a clear maximum. It corresponds to a distance of 12 nm between adjacent crystalline layers. The peak is not narrow. This shows that the lateral extension of the layers is not wide. The pattern is typical for the semicrystalline structure after non-isothermal oriented crystallization of common polyolefins. According to previous studies [57–60] of oriented polyolefin crystallization the first indication of crystallization in the SAXS pattern is a short meridional streak, related to a sequence of extended crystalline layers that are placed at random along the axis of the material (figure 4(a)). Thereafter the length of the streak starts to grow (figure 4(b)), indicating that the packing density of the layers increases in a random car-parking process [60–65]. Finally (figure 4(c)) a clear maximum develops at the tip of the meridional streak. The peak broadens and the ultimate 'two-point pattern' has developed. It has been found that the peak maximum emerges from the streak because secondary lamellae are created in the central plane [66] of each amorphous layer between the randomly placed primary lamellae. In summary, the injection-molded neat PP shows the common, fully developed nanostructure of PP crystallized from the melt. Thus it can be expected that the material shows the typical mechanical properties of neat PP.

Figure 3(b) presents the typical SAXS pattern from the skin region of all the injection-molded NCs. Here the PP scattering is represented by a meridional streak only (arrow). This finding is readily explained by an interruption of the crystallization during the stage of primary crystallization caused by the temperature quench at the surface of the rods. A pronounced long-period peak is not observed in the patterns from the scans. Thus the common arrangement of secondary crystalline domains is not found. Nevertheless, secondary crystallization must have happened in the NCs as well. This follows from comparison of the crystallinities $w_{c,PP}$ of the samples (table 1). The overall crystallinity of the NCs is almost as high as that of the neat PP. Thus with respect to the secondary crystalline domains the reasons for a missing long-period peak is probably continued random placement of (secondary) crystalline domains. This observed distortion of the PP nanostructure is coupled to the presence of the organoclay. The missing SAXS peak indicates that secondary nucleation no longer starts in a layer which is equidistant from the adjacent primary lamellae. It appears reasonable to assume that now nucleation becomes coupled to the random positions of MMT fragments. According to the literature, blending of MMT into PP leads to strong heterogeneous nucleation [22–24], and this effect is intensified by intercalation and partial exfoliation [7, 23]. Thus the nuclei density in the PP melt inoculated with MMT is most probably higher than that found in neat PP. As a consequence, even the sizes of the secondary domains should remain smaller and the domains less perfect in the NCs. Thus it appears reasonable that the PP matrix of the NCs exhibits deteriorated mechanical properties as compared to neat PP.

Figure 3(b) also shows an isotropic reflection that is not present in the patterns of neat PP. It is related to the stacking

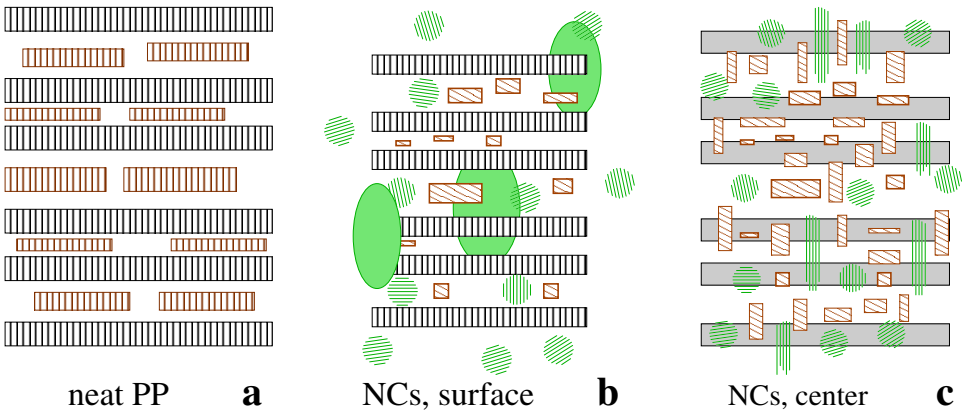


**Figure 5.** Visualization of the nanostructure models based on the fundamental SAXS features of figure 3. The local fiber axis is vertical.

of the silicate layers (spacing: 3.7 nm). In the n-scans from the skin region the layered clay particles exhibit no orientation. This finding can be explained if we assume that there exist not only large anisotropic clay flakes but also isotropic grainy clay fragments. Such grains cannot probe the shear field because of insufficient anisotropy. On the other hand, intact clay flakes located close to the rod surface may be oriented in such a way that they do not reflect in the n-scan. MMT particles reflect only, if the normal on the MMT layers is perpendicular to the direction of the x-ray beam.

Figure 3(c) shows the common SAXS pattern from the central region of the molded rods. Here we observe that a significant amount of clay platelets is oriented parallel to the direction of the flow. In addition, an isotropic background MMT-reflection is observed which probes MMT that has not oriented parallel to the flow. Again, the isotropic component may be explained by some grainy fragments. In our load-cycling study [28] we have postulated such material and have called it 'dust'. Now the isotropic scattering feature in the NC structure gradient supports our earlier explanation.

Let us discuss the scattering of the PP in the NCs. Nowhere the discrete scattering of a mature semicrystalline structure (like that from figure 3(a)) is observed. Moreover, in the core of the NCs there is not even a meridional streak from the primary lamellae. We assume that in the core this feature has been overgrown by the strong diffuse central scattering of already addressed secondary crystalline domains that are not arranged but placed at random.

Based on the SAXS data, simple models of the nanostructures of neat PP and the NCs are sketched (figure 5). In the drawings rectangular blocks indicate crystalline PP domains. Primary layers are laterally extended. In neat PP (figure 5(a)) secondary lamellae are placed in the centers of the gaps between the primary layers. In the SAXS this arranged placement generates a discrete peak. In the skin zone of the NC rods (figure 5(b)) the secondary crystallization appears at least partially suppressed. The secondary lamellae that may be formed are not placed in relation to the positions of the primary ones any more. Hashed circles indicate MMT grains that are seen 'edge on' in the n-scan. They generate the isotropic reflection of MMT. In the NCs such MMT grains determine, where secondary crystalline domains are formed. Green ellipses indicate extended MMT particles (flakes, platelets) in the proximity of the rod surface. They must be oriented more or less parallel to the rod surface. Thus they are not detected in the n-scans. In the center of the NCs (figure 5(c)) the stochastic secondary crystallization of PP has elapsed uninhibited and the corresponding strong diffuse scattering hides the relatively weak primary PP structure (gray layers in the background). Figure 5(c) sketches only those MMT particles (hashed circles and hashed ellipses) that contribute to the observed MMT scattering (isotropic ring plus equatorial peak).

A shortcoming related to our restricted set of samples must be mentioned. We cannot decide, if the deterioration of the PP crystallization process is a result of the MMT or of the added SEBS.

### *3.2. Variation of the scattering patterns of the composites along the residual webs*

Let us discuss the scattering patterns of the NCs taken along the machined webs. The patterns presented are already aligned with their local fiber axis pointing in vertical direction. The rotation angle that corrects the observed misorientation ($\phi_{\mathrm{corr}} = -\phi_{\mathrm{or}}$) is discussed below.

Figure 6 presents the SAXS patterns from the scanning experiments of the three composites. The left half of figure 6 shows the p-scan data. Obviously the variation of the composition changes the nanostructure gradient (column 1 is somewhat different from columns 2 and 3), but the modification of the MMT using a purified oligoester compound has little effect on the nanostructure gradient (columns 2 and 3 look nearly identical). The skin zone in which primary PP crystallization in oriented layers is observed is about 300 $\mu$m thick. The right half of figure 6 shows the n-scan data. The scattering intensity of the corresponding patterns is much lower than that of the p-scan patterns. Therefore different intensity scales have been chosen. Again, the use of a purified oligoester compound has no significant effect on the formed nanostructure. Only in few rows from the top anisotropy is found both in the n- and the p-scans. In this central zone reflecting MMT platelets probe the melt-flow direction. It is $\pm$250 $\mu$m wide. The p-scan

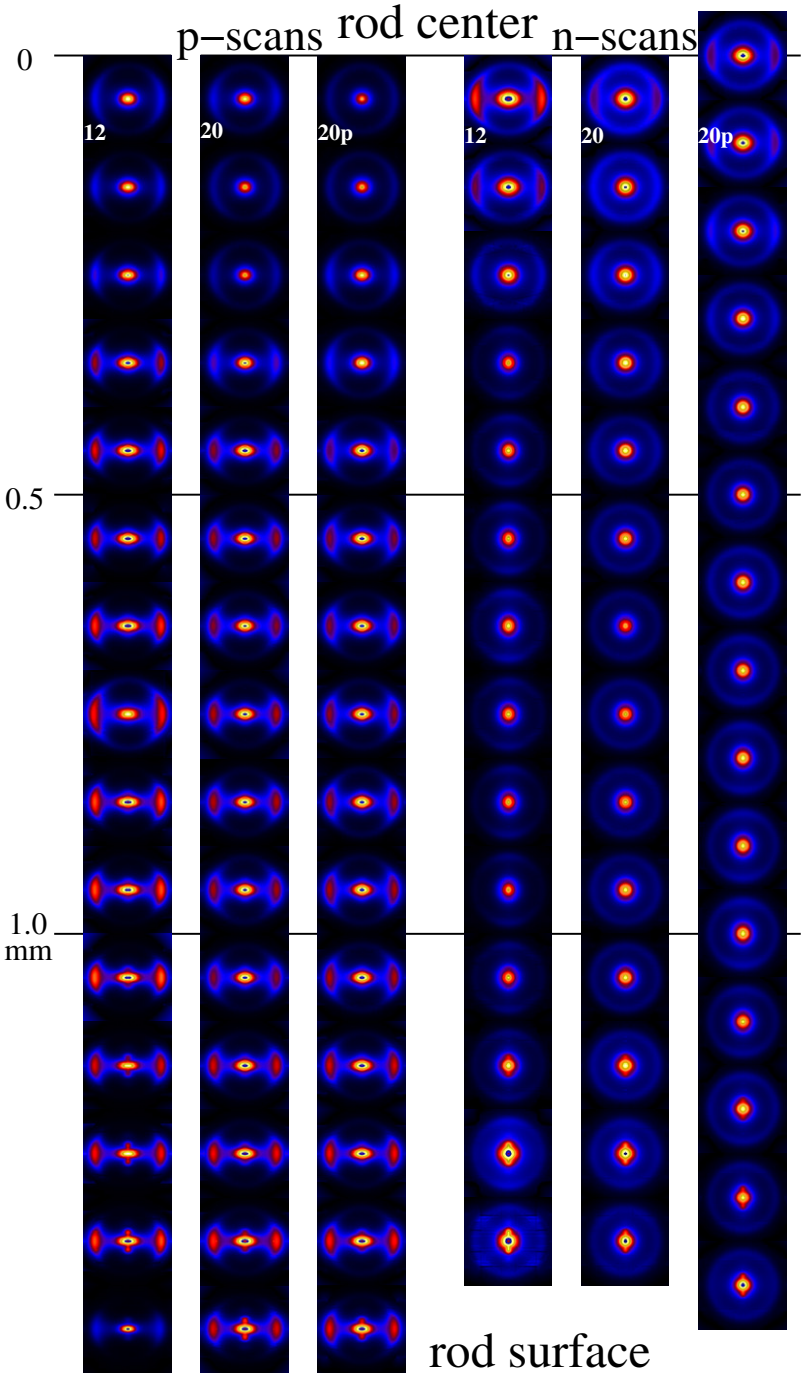


**Figure 6.** SAXS intensities log (log ($I$ ($s_{12}$, $s_3$))) of the three studied composites. All p-scans with the same white level $w_p$. All n-scans with white-level $w_n = 5\,w_p$, because here the scattering is weaker than in p-scans. The local fiber axis ($s_3$) is vertical. The patterns show the region $-0.38 \leqslant s_{12}, s_3 \leqslant 0.38\,\mathrm{nm}^{-1}$. Only half of the diameter data are shown, because the pattern sequence is symmetric with respect to the rod center. Each column is labeled by the last characters of the sample designation.

patterns from the rod surface (bottom patterns) show an anisotropic equatorial MMT peak, where the corresponding n-scan data are isotropic. This difference between the SAXS patterns of p- and n-scans is readily explained by a guiding effect of the mold wall on extended platelets of MMT. The corresponding 3D arrangement of the MMT particles in the NCs is sketched in figure 7. The top row of the sketch shows the wall of the mold represented by the segment of a hollow glass cylinder behind which MMT particles are arranged. The PP nanostructure is omitted. In the sketch the same structure is shown under three different angles. The first and the third sketch correspond to the alignment in a p-scan and in an n-scan, respectively. The corresponding scattering patterns are displayed below. The skin structure should be affected by the shear of the melt flowing along the wall of the mold. It causes anisotropic MMT platelets to align with their face parallel to the wall. Consequently, they are visible in p-scans, but not in n-scans.

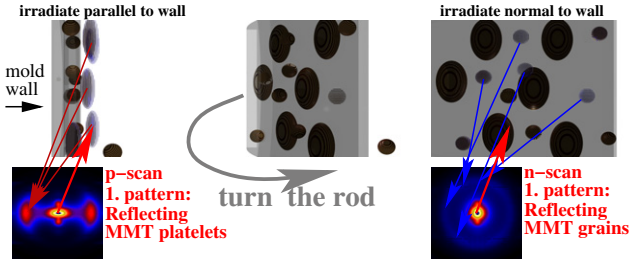


**Figure 7.** Close to the rod surface: unified three-dimensional (3D) model of the MMT structure that generates both the scattering features of the p-scan (left) and of the n-scan. The hollow 'glass cylinder' indicates the guiding wall of the mold.

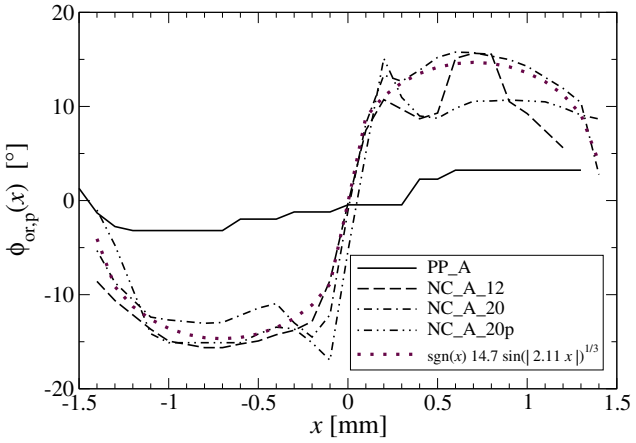


**Figure 8.** Variation of the fiber axis orientation, $\phi_{or,p}(x)$ , as a function of the position $x$ of the probed voxel in p-scans across the machined webs of the sample rods. Dotted curve: best nonlinear fit assuming a function of type $\phi_{or,p}(x) = \mathrm{sgn}(x)\ a_0\ \sin(|a_1 x|)^{1/n}$ with fixed $n$. Fit parameters are $a_0$ and $a_1$. Negative $\phi_{or,p}$ means that the mean platelet appears rotated clockwise (the scattering pattern is adjusted by counterclockwise rotation).

### *3.3. Away from the skin: orientation of the local fiber axis*

Close to the rod surface the axis of the MMT platelets is almost parallel to the wall. Proceeding inward this orientation is changing. The variation of the local fiber axis in the p-scans is presented in figure 8. A considerable difference between neat PP (PP_A) and the composites is observed. Everywhere in the neat PP the fiber axis is almost parallel to the cylinder axis. On the other hand, in the NCs the fiber axis varies considerably along the scan path. For all NCs the misorientation function $\phi_{or,p}(x)$ is similar. It can be approximated by the same analytical equation

$$\phi_{or,p}(x) = \mathrm{sgn}(x)\ \phi_{max}\ \sin\left(\pi\ \frac{|x|}{r}\right)^{1/3}, \qquad (1)$$

which is found empirically by systematic variation of the fixed exponent (1/2,1/3,1/4) and nonlinear regression with two free parameters ($a_0$ and $a_1$, cf figure 8). In equation (1) $r$ is the radius of the molded rod and $\phi_{max} = 14.7°$ is the maximum misorientation angle found in a p-scan. From the geometrical point of view equation (1) describes the orientation of those MMT platelets for which the layer-normal lies in the plane that is defined by the machined radius and by the axis of the injection-molded rod. Equation (1) represents a quantitative description of the 'numerical orientation prediction' reviewed by Altan [42] as sketched in his figure 6. Our data show that in the center the inclination of the MMT-platelets is inverted in a rather narrow zone. This core region coincides with the zone in which oriented MMT flakes are detected in the n-scans (cf Figure 6).

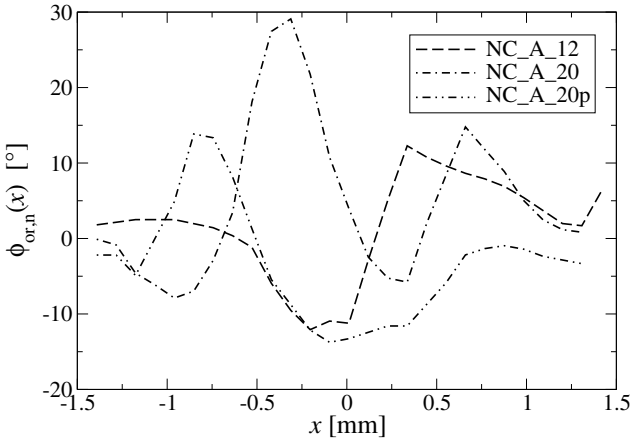


**Figure 9.** n-scans along slanted machined webs: variation of the local fiber axis orientation angle, $\phi_{or,n}(x)$, as a function of the radial position $x$ of the probed voxel.

In the n-scans a complex variation of the inclination angles is recorded. Figure 9 shows the result. The reason for the complex variation may be related to reduced significance of the data. Firstly, the geometry of the machined web is more complex with the n-scans (superposed upward movement along the rod that may lead to geometrical distortions of the path coordinate). Secondly, the overall intensity is lower by almost one order of magnitude. Thirdly, clear anisotropy is restricted to a narrow region, and this makes it more difficult to determine $\phi_{or,n}$.

### *3.4. Orientation distributions*

It has been demonstrated that the anisotropy of the MMT peak in the SAXS patterns from the n- and p-scans is varying across the rod diameter. Moreover, the variation in the n-scans is different from that in the p-scans. This means that even after correction for the tilt of the local principal axis there is no local fiber symmetry in the NCs with respect to the arrangement of the MMT flakes.

Thus the conditions of strict uniaxial orientation and of fiber symmetry are not met. Nevertheless, we propose to visualize the MMT orientation by a UOP. Thus what we compute a *pseudo* UOP [37, 50]

$$f_{or,ps} = \frac{\int_0^{\pi/2} I(\alpha, s_m)\ \frac{1}{2}\left(3\cos^2\alpha - 1\right)\sin\alpha\,\mathrm{d}\alpha}{\int_0^{\pi/2} I(\alpha, s_m)\ \sin\alpha\,\mathrm{d}\alpha}. \qquad (2)$$

Here $I(\alpha, s_m)$ is a circular intensity cut through the maximum (at $s = s_m$) of the MMT peak in the SAXS patterns. $\alpha$ is the angle between the principal axis and the direction in which the intensity is probed. Because fiber symmetry is violated, we obtain different curves from n- and p-scans.

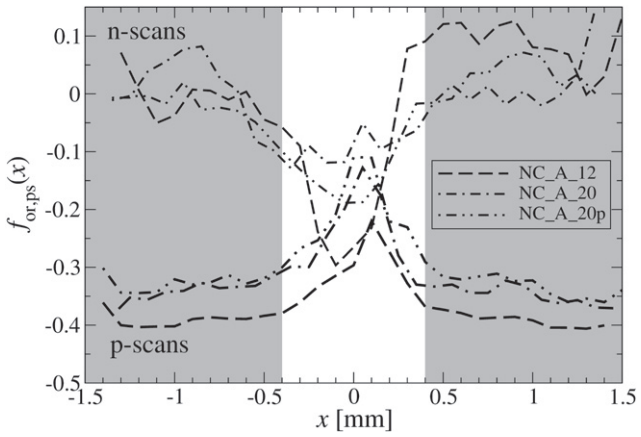


**Figure 10.** Widths of the MMT-orientation distributions in terms of a *pseudo* uniaxial orientation factor $f_{or,ps}(x)$ in n- and p-scans. Outside the central region $|x| > 0.4$ local fiber symmetry is severely violated.

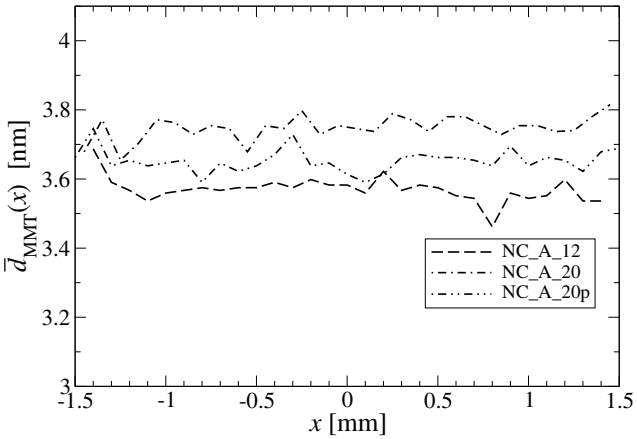


**Figure 11.** Variation of the most probable spacing $\bar{d}_{MMT}$ among the MMT layers along the distance $x$ from the center of the injection-molded rods.

Figure 10 presents the corresponding results. At the surface of the injection-molded rods ($x \approx \pm 1.5$ mm, i.e. $x = r$) the reflections of the p-scans show a narrow maximum at the equator. If they were infinitely narrow, we would compute $f_{or,ps} = -0.5$. Isotropic rings equate to $f_{or,ps} = 0$. This case is observed for the n-scans at $x \approx r$. In the p-scans close to the rod surface the orientation distribution of the MMT flakes is very narrow. In the center of the rods the perfection of flake orientation is lower. Here some influence of the NC composition is indicated. In the NC with 12 wt% SEBS the flake orientation is more anisotropic than in the NCs with 20 wt% SEBS.

The orientation-anisotropy gradient retrieved from the n-scans is characterized by curves that start from the isotropic state and slope down toward the rod center. They describe the complementary view of the p-scans. Initially no anisotropic flakes are visible, because the proximity of the wall has forced these flakes to orientate in such a way that they do no not cause a reflection. Close to the center of the rods both the widths of the orientation functions and the intensities of the scattered patterns are similar for n- and p-scans. In figure 10 this region is indicated by a white background. Here the effect of the mold wall appears to be small. Vice versa, the zone in which the MMT structure is varying by the proximity of the mold wall is almost 1 mm thick.

The angular position $s_m$ of the MMT reflection is a measure of the most-probable interlayer distance, $\bar{d}_{MMT} = 1/s_m$. Figure 11 presents $\bar{d}_{MMT}(x)$ as a function of the distance $x$ from the rod center for the three studied composites. The data are taken from the p-scans. The curves obtained from the n-scans yield identical average values, but are more noisy. For each sample $\bar{d}_{MMT}(x) = \text{const}$ is found. There is no core–skin gradient. Nevertheless, there are slight but significant variations among the composites. The material with the lowest SEBS content (NC_A_12) exhibits the smallest intercalation with $\bar{d}_{MMT} = 3.55$ nm. In the material NC_A_20p the distance appears widened by 0.1 nm, and an additional slight widening is observed for the sample NC_A_20. From a technical point of view these differences appear small.

## 4. Conclusions

In injection-molded parts of neat polymers the domain orientation is often nearly constant [38, 49]. Obviously much more complex structure gradients can occur in parts of composites, if the composites contain flake-shaped nanoparticles. In this case the risk of misinterpretation is considerable, if the solid part is irradiated by a microbeam and the scattering images are interpreted directly [67, 68]. Then even a computed-tomography method [35, 36] yields incorrect results.

For such complex structure gradients in cylindrical samples, a method has been proposed to machine the rods before scattering data are extracted. Very thin webs are machined in two principal directions, scanned by an x-ray microbeam and corresponding scattering patterns are compared to each other. In this way the structure gradient of the filler-particle orientation can be described semi-quantitatively.

In the system studied, the addition of MMT obviously leads to deterioration of the PP structure. The secondary crystallization of PP is no longer guided by the primary lamellae, but appears to start from MMT fragments. However, there are also x-ray macrobeam studies on PP/MMT composites, in which the PP nanostructure appears less distorted [25, 27]. For such a material, a respective microbeam study would show whether the regular PP nanostructure is limited to the skin zone or whether it runs through the entire injection molding. Such comparative studies could expand the knowledge on the nucleating effect of non-exfoliated MMT to PP.

Aiming to develop an improved PP composite, there are several parameters and procedures that appear to be worth considering. First, the structure formation in PP appears highly dependent on its cooling rate [69] and on comonomers in the chain [70]. Studies that monitor fast solidification benefit from a concept of metallurgy that has been introduced to polymer science by Spruiell and White [71], the so-called continuous cooling transformation and related plots [69, 70]. As long as the NC components are joined by melt-mixing, it may remain difficult to avoid the introduction of nucleating grainy clay besides the desired exfoliated sheets. Then it

would make sense to modify the nucleating surface of the grains. Promising approaches are presented in studies [13, 72, 73] that turn attention to the tailoring of the nucleation efficiency of clay particles. Moreover, there is a recent report [74, 75] about a solvent-mixing method that promises complete exfoliation of layers.

## Acknowledgments

Farhad Jokari Sheshdeh is acknowledged for his help with the data analysis. The authors thank the Hamburg Synchrotron Radiation Laboratory (HASYLAB) for beam time granted in the frame of project I-2011-0087. Preparation of the materials had been supported by the seventh framework program of the European Union (Project NANOTOUGH FP7-NMP-2007-LARGE).

## References

[1] Alsewailem F D 2012 *Open Macromol. J.* **6** 19
[2] Pfaendner R 2010 *Polym. Degrad. Stab.* **95** 369–73
[3] Leuteritz A, Pospiech D, Kretzschmar B, Willeke M, Jehnichen D, Jentzsch U, Grundke K and Janke A 2003 *Adv. Eng. Mater.* **5** 678–81
[4] Goettler L A, Lee K Y and Thakkar H 2007 *Polym. Rev.* **47** 291–317
[5] Chrissopoulou K and Anastasiadis S H 2011 *Eur. Polym. J.* **47** 600–13
[6] Mittal V 2012 *Open Macromol. J.* **6** 37–52
[7] Vu Y T, Rajan G S and Mark J E 2004 *Polym. Int.* **53** 1071–7
[8] McGenity P M, Hooper J J, Paynter C D, Riley A M, Nutbeem C, Elton N J and Adams J M 1992 *Polymer* **33** 5215–24
[9] Ma J, Zhang S, Qi Z, Li G and Hu Y 2001 *J. Appl. Polym. Sci.* **83** 1978–85
[10] Pozsgay A, Fráter T, Papp L, Sajó I and Pukánszky B 2002 *J. Macromol. Sci.* B **41** 1249–65
[11] Maiti P, Nam P H, Okamoto M, Kotaka D, Hasegawa N and Usuki A 2002 *Polym. Eng. Sci.* **42** 1864–71
[12] Li J, Zhou C and Gang W 2003 *Polym. Test.* **22** 217–23
[13] Zheng W, Lu X, Toh C L, Zheng T H and He C 2004 *J. Polym. Sci.* B **42** 1810–6
[14] Sun T, Chen F, Dong X and Han C C 2008 *Polymer* **49** 2717–27
[15] Dlugosz J, Fraser G V, Grubb D, Keller A and Odell J A 1976 *Polymer* **17** 471–80
[16] Bitter I, Kaufman A E and Sato M 2001 *IEEE Trans. Vis. Comput. Graph.* **7** 195–206
[17] Zhu P W and Edward G 2003 *Macromol. Mater. Eng.* **288** 301–11
[18] Šmit I, Musil V and Švab I 2004 *J. Appl. Polym. Sci.* **91** 4072–81
[19] Lipp J, Shuster M, Terry A E and Cohen Y 2008 *Polym. Eng. Sci.* **48** 705–10
[20] Domenech T, Peuvrel-Disdier E and Vergnes B 2013 *Compos. Sci.* **75** 7–14
[21] Lertwimolnun W and Vergnes B 2007 *Polym. Eng. Sci.* **47** 2100–9
[22] Causin V, Marega C, Saini R, Marigo A and Ferrara G 2007 *J. Thermal Anal. Calor.* **90** 849–57
[23] Liu X, He A, Du K and Han C C 2009 *J. Polym. Sci.* B **47** 2215–25
[24] Rozanski A, Monasse B, Szkudlarek E, Pawlak A, Piorkowska E, Galeski A and Haudin J M 2009 *Eur. Polym. J.* **45** 88–101
[25] Stribeck N, Zeinolebadi A, Ganjaee Sari M, Botta S, Jankova K, Hvilsted S, Drozdov A, Klitkou R, Potarniche C G, Christiansen J d and Ermini V 2012 *Macromolecules* **45** 962–73
[26] Koo C M, Kim S O and Chung I J 2003 *Macromolecules* **36** 2748–57
[27] Kim J H, Koo C M, Choi Y S, Wang K H and Chung I J 2004 *Polymer* **45** 7719–27
[28] Zeinolebadi A, Stribeck N, Vuluga Z, Schloen C, Botta S and Ganjaee Sari M 2013 *Polym. Adv. Technol.* **24** 693–704
[29] Riekel C, Burghammer M and Müller M 2000 *J. Appl. Crystallogr.* **33** 421–3
[30] Müller M, Czihak C, Burghammer M and Riekel C 2000 *J. Appl. Crystallogr.* **33** 817–9
[31] Nozue Y, Shinohara Y and Amemiya Y 2007 *Polymer J.* **39** 1221–37
[32] Ice G E 2011 *Science* **334** 1234–9
[33] Loidl D, Peterlik H, Paris O, Müller M, Burghammer M and Riekel C 2005 *J. Synchrotron Radiat.* **12** 758–64
[34] Riekel C 2000 *Rep. Prog. Phys.* **63** 233–62
[35] Stribeck N, Nöchel U and Almendárez Camarillo A 2008 *Macromol. Chem. Phys.* **209** 1976–82
[36] Stribeck N, Nöchel U, Fakirov S, Feldkamp J, Schroer C, Timmann A and Kuhlmann M 2008 *Macromolecules* **41** 7637–47
[37] Hermans J J, Hermans P H, Vermaas D and Weidinger A 1946 *Rec. Trav. Chim. Pays-Bas* **65** 427–47
[38] Wang Y D and Cakmak M 2001 *Polymer* **42** 4233–51
[39] Singh P and Kamal M R 2004 *Polym. Compos.* **10** 344–51
[40] Koerner H, Price G, Pearce N A, Alexander M and Vaia R A 2004 *Nature Mater.* **3** 115–20
[41] Xavier S F, Schultz J M and Friedrich K 1990 *J. Mater. Sci.* **25** 2411–20
[42] Altan M C 1990 *J. Thermoplast. Compos. Mater.* **3** 275–313
[43] Halpin J C 1967 AFML TR-67-423 p. 2031
[44] Mori T and Tanaka K 1973 *Acta Metall.* **21** 571–4
[45] Kantz M R, Newman H D and Stigale F H 1972 *J. Appl. Polym. Sci.* **16** 1249–60
[46] Vuluga Z, Panaitescu D M, Radovici C, Nicolae C and Iorga M D 2012 *Polym. Bull.* **69** 1073–91
[47] Nogales A, Hsiao B S, Somani R H, Srinivas S, Tsou A H, Baltà Calleja F J and Ezquerra T A 2001 *Polymer* **42** 5247–56
[48] Stribeck N 2010 *IOP Conf. Ser.: Mater. Sci. Eng.* **14** 012003
[49] Schroer C G, Kuhlmann M, Roth S V, Gehrke R, Stribeck N, Almendarez Camarillo A and Lengeler B 2006 *Appl. Phys. Lett.* **88** 164102
[50] Stribeck N 2007 *X-Ray Scattering of Soft Matter* (Heidelberg: Springer)
[51] Buhmann M D 2000 *Acta Numer.* **9** 1–38
[52] Nedevschi S 2011 Image-processing laboratory 6: border tracing (http://ftp.utcluj.ro/pub/users/nedevschi/IP/IP_Labs_2011/ipl_06e.pdf)
[53] MATLAB 2010 version 7.10.0 (Natick, MA: The MathWorks)
[54] VNI 2007 *Pv-Wave Manuals* version 7.5 (Houston, TX: VNI)
[55] Stribeck N 2001 *J. Appl. Crystallogr.* **34** 496–503
[56] Stribeck N, Buzdugan E, Ghioca P, Serban S and Gehrke R 2002 *Macromol. Chem. Phys.* **203** 636–44
[57] Stribeck N, Nöchel U, Almendárez Camarillo A, Roth S V, Dommach M and Bösecke P 2007 *Macromolecules* **40** 4535–45
[58] Stribeck N, Almendarez Camarillo A, Cunis S, Bayer R K and Gehrke R 2004 *Macromol. Chem. Phys.* **205** 1445–54
[59] Stribeck N 2004 *Macromol. Chem. Phys.* **205** 1455–62
[60] Stribeck N, Almendarez Camarillo A and Bayer R 2004 *Macromol. Chem. Phys.* **205** 1463–70
[61] Rényi A 1958 *Publ. Math. Inst. Budapest* **3** 109–25
[62] Rényi A 1963 *Sel. Transl. Math. Stat. Prob.* **4** 203–18

[63] Burgos E and Bonadeo H 1987 *J. Phys. A: Math. Gen.* **20** 1193–204
[64] Bonnier B, Boyer D and Viot P 1994 *J. Phys. A: Math. Gen.* **27** 3671–82
[65] Stribeck N, Bayer R, Almendarez Camarillo A, Bösecke P and Gehrke R 2004 *Proc. Am. Chem. Soc. PMSE Prepr.* **91** 695–6
[66] Garcia Gutierrez M C, Rueda D, Baltá Calleja F J, Stribeck N and Bayer R K 2001 *J. Mater. Sci.* **36** 5739–46
[67] Riekel C and Engström P 1995 *Nucl. Instrum. Methods Phys. Res.* **B97** 224–30
[68] Paris O, Li C, Siegel S, Weseloh G, Emmerling F, Riesemeier H, Erko A and Fratzl P 2007 *J. Appl. Crystallogr.* **40** S466–70
[69] Choi C H and White J L 2000 *Polym. Eng. Sci.* **40** 645–55
[70] Cavallo D, Portale G, Balzano L, Azzurri F, Bras W, Peter G W and Alfonso G C 2010 *Macromolecules* **43** 10208–12
[71] Spruiell J E and White J L 1975 *Polym. Eng. Sci.* **15** 660–7
[72] Chua Y C and Lu X 2007 *Langmuir* **23** 1701–10
[73] Dai X, Zhang Z, Wang C, Ding Q, Jiang J and Mai K 2013 *Composites Part A* **49** 1–8
[74] Wang Q and O'Hare D 2013 *Chem. Commun.* **49** 6301–3
[75] Wang Q, Undrell J P, Gao Y, Cai G, Buffet J C, Wilkie C A and O'Hare D 2013 *Macromolecules* **46** 6145–50